

Contents lists available at ScienceDirect

Journal of Energy Chemistry

journal homepage: www.elsevier.com/locate/jechem

Dual-shell silicate and alumina coating for long lasting and high capacity lithium ion batteries

Marcos Lucero ^{a,1}, Tucker M. Holstun ^{a,1}, Yudong Yao ^b, Ryan Faase ^a, Maoyu Wang ^a, Alpha T. N'Diaye ^c, David P. Cann ^d, Joe Baio ^a, Junjing Deng ^{b,*}, Zhenxing Feng ^{a,*}

- ^a School of Chemical, Biological, and Environmental Engineering, Oregon State University, Corvallis, OR 97331, United States
- ^b Advanced Photon Source, Argonne National Laboratory, Argonne, Illinois 60439, United States
- ^cAdvanced Light Source, Lawrence Berkeley National Laboratory, Berkeley, California 94720, United States
- ^d Materials Science, School of Mechanical, Industrial, and Manufacturing Engineering, Oregon State University, Corvallis, OR 97331, United States

ARTICLE INFO

Article history: Received 31 May 2021 Revised 4 November 2021 Accepted 8 November 2021 Available online 16 November 2021

Keywords: Lithium cobalt oxide Surface coating Sol-gel Silicate

Alumina X-ray absorption spectroscopy

ABSTRACT

Here we demonstrate a theory-driven, novel dual-shell coating system of Li₂SrSiO₄ and Al₂O₃, achieved via a facile and scalable sol-gel technique on LiCoO2 electrode particles. The optimal thickness of each coating can lead to increased specific capacity (~185 mAh/g at 0.5C-rate) at a cut-off potential of 4.5 V, and greater cycling stability at very high C rates (up to 10C) in half-cells with lithium metal. The mechanism of this superior performance was investigated using a combination of X-ray and electron characterization methods. It shows that the results of this investigation can inform future studies to identify still better dual-shell coating schemes, achieved by such industrially feasible techniques, for application on similar, nickel-rich cathode materials.

© 2021 Science Press and Dalian Institute of Chemical Physics, Chinese Academy of Sciences. Published by ELSEVIER B.V. and Science Press. All rights reserved.

1. Introduction

Lithium-ion batteries (LIBs) containing layered lithium transition metal oxide cathodes, generally denoted as LiMO2 (M refers to transition metals), have seen wide scale application in portable electronics and electric vehicles due to their excellent cycling stability and comparatively high energy density [1-3]. However, electric vehicles at a comparable cost and travel range to their petroleum burning counterparts, and grid-scale energy storage outside fringe-cases, require secondary (i.e., rechargeable) batteries with higher energy density, longer lifespans, and lower cost [4-6]. While solid-state electrolytes and more experimental cathode compositions are being explored at lab-scale, the imminence of the deployment of electric vehicles and stationary storage still heavily rely on the improvement of the existing LIB technology, particularly on cathodes such as LiCoO₂ [7]. The current LIBs are operated at the voltage window of 3.0-4.2 V with ~140 mAh/g, which is barely sufficient to allow affordable electric vehicles

E-mail addresses: junjingdeng@anl.gov (J. Deng), zhenxing.feng@oregonstate. edu (Z. Feng).

(e.g., Nissan Leaf) to drive distances ~80 miles [5,8]. Several important barriers such as energy density, capacity fading, and charging rates must still be further improved.

The reversible capacity of LiCoO2 (LCO) results from the deintercalation of roughly half of the lithium ions, $Li_{1-x}CoO_2$ (0 < x < 0.5), from the lattice at a cut-off voltage of 4.2 V [9-11]. To draw more capacity from these cells, a higher cutoff voltage must be employed. If the cutoff voltage is raised, the capacity can be increased to closer to the theoretical value for LCO of 272 mAh/g. The trade-off to the increased energy density when operating above 4.2 V, is the quick degradation of the battery. Above this critical threshold, the initial capacity achieved is around 180 mAh/g, but rapidly declines within a few cycles [12]. It has been shown via theoretical calculations and post cycling analysis that the rapid performance degradation is due to structural changes, predominantly layered to spinel and rock salt, upon more complete removal of lithium from the host structure. Also, spectroscopic analysis has revealed increased dissolution rate of cobalt out of the cathode and into the electrolyte during high voltage cycling (i.e., charging to >4.3 V) [13–16]. This dissolution of transition metals from the cathode has been found to correspond to a greater rate of hydrofluoric acid (HF) formation from decomposition of the LiPF₆ electrolyte and corrosion at the surface of cathode particles [17]. As such, charging to high voltages (i.e., >4.3 V) is not practical

^{*} Corresponding author.

¹ These authors contributed equally to this work.

unless the cells can be stabilized (i.e., crystal structure, surface chemistry) during deep cycling.

Cathode stability plays such a crucial role in the lifetime of a battery. Much research has been focused on identifying functional coatings to prevent degradation of the battery cells. The addition of metal oxides to the surface of LCO has been shown countless times to provide an improvement in the stability through repeated cycling to 4.5 V [18-20]. In particular, Al₂O₃ is well documented as an effective cathode coating on both LCO and LiNi_xMn_vCo_{1-x-v}-O₂ chemistries [21]. The effectiveness of this coating, and similar metal oxides is thought to be owed to its sacrificial reaction with corrosive HF, repulsion, and separation of cathode surface from byproducts of organic electrolyte solvents, prevention of Co leaching and sufficient lithium-ion diffusivity [20,22]. Binary oxides such as Al₂O₃ are unlikely to be the best choice of coating material, as Al₂O₃ is not a good ion conductor with limited Li diffusivity only after the lithium doping that occurs upon cycling [23], and it does not have good mechanical flexibility to comply with large volume change of the cathode during Li insertion/extraction. Through a reaction model based on density functional theory, Aykol et al. [24] have screened more than 130000 oxide materials which can act as physical barriers to electrolytes, HF, and coatings which can scavenge HF. Guided by this high-throughput screening coating materials based on high HF reactivity, low reaction potential with cathode materials, electrochemical stability, and low mineral cost, Aykol et al. [24] identified Li₂SrSiO₄ (LSSO) as one of the thermodynamically and optimized coating material for LCO.

Many methods have been developed for coating electrode materials, one of which includes atomic layer deposition (ALD). This technique has been utilized for depositing conformal, thin layers $(\sim 1 \text{ nm})$ of materials onto electrodes [25]. Unfortunately, ALD is a process that has proven slow, small-scale, and expensive due to the specialized equipment and precursors required, making it impractical for application in wide-scale production of cathode material [26]. Previously, we have demonstrated the ease of the sol-gel method for coating Al₂O₃ to the surface of LCO. The sol-gel coating methods produce less uniform surface coatings, however the simplicity of the method makes it more industrially feasible. The thickness of the coating layers can range from 10 to 100 nm rather than ~1 nm for ALD, but non uniformities such as areas of thinner coating or bare regions may ease ionic resistance enough that this disadvantage is outweighed by the challenges of ALD. Furthermore, there is nearly no restriction on materials composition when using sol-gel, which thus makes it feasible for coating various promising candidate materials other than Al₂O₃ on LCO cathode.

In this article, we have successfully synthesized and coated the theoretically predicted LSSO on LCO cathode using the sol-gel method and identified the shortcomings of LSSO in battery applications. We further applied dual shell coating of LSSO and Al_2O_3 , resulting in LCO cathode capable of cycling from 3.0 to 4.5 V with higher initial capacity of \sim 185 mAh/g, and greater stability over 500 cycles and very high C-rate (10C) cycling than Al_2O_3 alone. The mechanism by which this dual coating out-performs similarly produced single coatings was investigated using a combination of electron and X-ray microscopy, as well as X-ray spectroscopy. It is hoped that the elucidated failure mechanisms of these coatings may help identify still better coating schemes achievable by easily scalable coating methods.

2. Experimental

2.1. Synthesis and coating

The synthesis of LSSO was achieved using a sol-gel method modified from a previous method, and its phase purity was confirmed by X-ray diffraction (XRD) (see discussion later). Both pure LSSO samples and coated material were produced from the same sol-gel precursor. The precursor solution was made from stoichiometric mix of a 10% excess of LiNO3 along with stoichiometric Sr (NO3)2 and tetraethyl orthosilicate (TEOS) in an equal part mixture of deionized water and ethanol. Next, the solution's pH was adjusted to 0.7 to promote gel formation. This mixture was then mixed and heated to 60 °C while covered for 24 h to form the universal precursor solution. Coatings of Al2O3 were created via a similar technique, using the same procedure as reported before, with aluminum isopropoxide as the aluminum source and gelling agent. Coatings of Li4SiO4 (LSO) were made by replacing the stoichiometric quantity of Sr with more Li.

To produce LSSO samples, the gel was dried, pulverized and calcined. To coat cathode particles, the appropriate volume of either precursor solution to achieve a certain wt% of LSSO or Al₂O₃ was added to cathode powder (LCO purchased from Sigma-Aldrich without further purification) and mixed by hand in a mortar and pestle for 1 h with periodic additions of ethanol to facilitate mixing. The cathode powder was allowed to dry while mixing such that dry powder with gel deposited on it was obtained. This powder was then calcined by the same procedure as LSSO samples for both LSSO and Al₂O₃ coated cathode powder: 5 °C/min heating to 450 °C, a hold at 450 °C for 3 h, 10 °C/min heating to 600 °C, a hold at 600 °C for 3 h, and finally cooling at 10 °C/min to room temperature. The resulting coated cathode material was then pulverized by hand for use in coin cells. If the cathode powder being produced was to be dual-coated, the powder obtained after the first calcination was recovered and coated by the same technique with the other material just as bare cathode powders would be.

2.2. Electrochemical measurement

Cathodes for use in coin cells were created with 80 wt% cathode powders, 10 wt% carbon C45, and 10 wt% polyvinylidene fluoride (PVDF) by manual pulverization and slurry casting in N-methyl-2-pyrrolidone (NMP) onto aluminum foil, followed by drying under vacuum at 70 °C for 12 h. Resulting cathodes with an active mass of approximately 3-4 mg and active mass loading of ~4.45 mg/cm² were assembled in an argon-filled glove-box with lithium metal foil reference electrodes in CR2032 coin cells with glass fiber separators and 1 M LiPF₆ in EC:DEC (1:1) electrolyte. The cells (halfcell configuration) were operated over a voltage window of 3.0-4.5 V at C rates of 0.2-10C on a LANHE test rack. C is rate defined relative to charging or discharging cells with a capacity of 180 mAh/g in 1 h, 1C: 180 mA/g. Full cell measurements used the same electrolyte and cathodes mentioned previously and were paired with graphite anodes with a composition of 92% Superior SLC graphite, 6% PVDF and 2% carbon C45. The N/P ratio for the full cell coin cells ranged from 1.1 to 1.2 and operated in a voltage window of 2.5-4.45 V. Cyclic voltammetry (CV) scans were collected at a rate of 10^{-4} V/s for three full charge and discharge cycles.

2.3. SEM, XPS, XRD

Scanning electron microscopy (SEM) images of electrode materials were taken at the OSU Electron Microscopy Facility using a field emission SEM (FEI Quanta600) at 5 kV and a working distance of 10.5 mm. X-ray photoelectron spectroscopy (XPS) data were collected at the Oregon State University (OSU) Northwest Nanotechnology Infrastructure using a PHI 5600 equipped with a Monochromatic Al K X-ray source (1486.6 eV). X-ray diffraction was performed on Rigaku Ultima instrument using Cu K_{α} source (λ = 1.5406 Å)

2.4. XAS and ptychography

Hard X-ray absorption spectroscopy (hXAS) at the Co K-edge was performed at beamline 9BM of the Advanced Photon Source (APS) of Argonne National Laboratory (ANL). A Co metal reference was used as a standard to properly calibrate the energy. Both Co Kedge X-ray absorption near edge structure (XANES) and extended X-ray absorption fine structure (EXAFS) were measured under fluorescence mode by a Vortex ME4 detector. Soft XAS (sXAS) at Co Ledge was performed at Co L-edge and O K-edge using both fluorescence and electron yield modes at beamline 6.3.1 of Advanced Light Source (ALS) of Lawrence Berkeley National Laboratory (LBNL) and beamline 7-ID-1 (SST-1) of National Synchrotron Light Source (NSLS) II of Brookhaven National Laboratory (BNL), All XAS data analysis was performed with Athena software package to extract XANES and EXAFS. The EXAFS data were modelled using Artemis software package in k and R space in the ranges of [3–13] $Å^{-1}$] and [1–4.5 Å], respectively. An integral method was used to determine the Co oxidization state with Co K-edge XANES.

Simultaneous X-ray fluorescence and ptychography [27,28] were collected at the Advanced Photon Source at beamline 2-ID-D in Argonne National Laboratory. A monochromatic X-ray beam at 8.8 keV was focused by a Fresnel zone plate with an outer zone width of 70 nm, producing a focus spot of around 150 nm on samples. A Vortex silicon drift detector was placed on the right side of the sample at 75 degrees with respect to the beam propagation direction to record the fluorescence signals, while a Dectris Eiger X 500K pixel array detector locating 1.32 m downstream of the sample was used to collect coherent diffraction patterns. The step size of 2D fly-raster scans on the sample was 80 nm for both *X* and *Y* directions, yielding a pixel size of 80 nm on elemental maps. In addition, ptychographic images were reconstructed from coherent diffraction patterns with a pixel size of about 10 nm.

3. Results

3.1. Electrochemical performance

The predicted properties of the LSSO coating were tested in LCO cells with several different LSSO coating thicknesses at a rate of 0.5C with an upper and lower cutoff voltage of 4.5 and 3.0 V, respectively. Coatings of 0.25, 0.5, and 1 wt% LSSO by weight on LCO all yielded cycling performance similar to that of uncoated material (see Fig. S1). Despite an initial discharge capacity of \sim 196 mAh/g, the capacity degraded rapidly, approaching values of non-coated LCO at the same cycling number. The LSSO coating did not improve the capacity retention of LCO but did result in an initial increase in capacity prompting further investigation into its application as a coating material for LCO. We then experimented with dual-shell coatings using both LSSO and Al₂O₃ to achieve the higher capacities obtained from the 0.5 wt% LSSO or (0.5 LSSO) coating and the capacity retention obtained from coatings of Al₂O₃. Since the dual coatings require a two-step procedure, we tested the order in which the coatings were added to the cathode particles. In the 0.5 wt% Al_2O_3 0.5 wt% LSSO coating, with Al_2O_3 as the inner and LSSO as the outer coating, the capacity retention, and discharge capacity was identical to the 0.5 wt% Al₂O₃ or (0.5 Al₂O₃) coating, while the 0.5 wt% Al₂O₃ 0.5 wt% LSSO had similar capacity retention but lower capacities (see Fig. S1). This revealed that having an inner layer of Al₂O₃ negated any benefits from the LSSO coating. Reversing the coating scheme and having an inner coating of LSSO and an outer coating of Al₂O₃, the benefits of the LSSO appear in the electrochemical data. In LCO with a coating of 0.25 wt% LSSO 0.25 wt% Al₂O₃ (dual), hereafter referred to as the dual coating, the discharge capacity is increased, and the capacity

retention is superior to the other coating schemes investigated in this work, including single coatings and uncoated LCO (Fig. 1a). Comparing the performance of this coating orientation with different coating thicknesses demonstrated that the dual coating (0.5 wt % in total) provided the greatest capacity and cycle life in coin cells. The initial discharge capacity of ~187 mAh/g was lost at an average rate of 0.07% per cycle at 0.5C for 500 cycles, or 64% retention (Fig. 1c). Unlike material coated with Al₂O₃, the dual coating allowed for tolerance of several charges in a row at 10C, with capacity utilization of ~93% when returned to 0.5C (Fig. 1b). Cyclic voltammetry (CV) measurements during the first three cycles reveal greater stability for the dual coated over 0.5 Al₂O₃ and bare LCO showing (Fig. S2). Our full-cell tests using graphite anode also show the similar trend as half-cell tests (Fig. S10), namely the performance of cathode with dual coating surpassing that of uncoated LCO or LCO coated with LSO. These results show that the dual coating with both an inner layer of LSSO, and an outer layer of Al₂O₃. cathode material with superior capacity, rate capability, and cycle life, can be produced. This suggests that there is indeed a complementary effect between the two coating materials, in which each is performing functions that the other is less capable of.

3.2. In-house characterization

Powder XRD was performed on an electrode powder with an excess coating of LSSO (50 wt% LSSO) on the cathode powder. This experiment was conducted to determine the crystallinity of the coating material once applied to the surface of LCO. In Fig. 2(a), the measured diffraction data match the peaks from both crystalline LCO and LSSO, revealing that the coating is in the expected crystalline phase and that the sol-gel coating procedure is viable [14]. XRD is also measured for uncycled bare, 0.5 Al₂O₃, 0.5 LSSO, and dual coated material. As seen in Fig. 2(b), the material with surface coatings with a total of 0.5 wt% coatings can be indexed to the R3m space group of LCO [29,30]. Synchrotron XRD further confirms the crystalline phase of LCO for the coated sample and reveals no impurity (Fig. S3). The features from LSSO or Al₂O₃ cannot be observed in the diffractogram, indicating a sub-micron coating layer. Due to the thin surface coating, we turned to XPS to measure the change in the Co 2p spectra before and after cycling. The Co 2p region of 770-810 eV remains primarily unchanged for the uncycled coated samples, with the Co $2p_{3/2}$ and Co $2p_{1/2}$ retaining their position at \sim 780.7 and \sim 796.0 eV. After cycling, the data quality decreases dramatically, possibly due to the formation of an interphase, which would reduce photoelectrons escaping the sample and Co leeching [31]. Broadening of the $2p_{3/2}$ and the increasing satellite peak area left of Co $2p_{3/2}$ is seen in the bare and 0.5 LSSO, suggesting a reduction of Co from +3 to an oxidation state of +2 (Fig. S4) [32]. Since it was difficult to determine this from XPS due to an incomplete data set, we turned to another surface sensitive technique discussed later. The morphology of the powders is observed through SEM, and the bare and coated LCO powders consist of particles on the order of 10–20 μm (Fig. S5).

3.3. Synchrotron characterization

To further elucidate the surface morphology and elemental composition of the coating, we turned to simultaneous X-ray fluorescence microscopy and ptychography [27,28]. The sub-micron X-ray beam in this combined measurement can detect elemental information from samples at a spatial resolution limited by the focused beam size (150–200 nm). The phase information provided by ptychography is sensitive to the density variation of materials at hard X-rays, which is a powerful tool to probe the interior and surface structures of the particles at a spatial resolution not limited by the focused spot. These measurements were performed for pristine

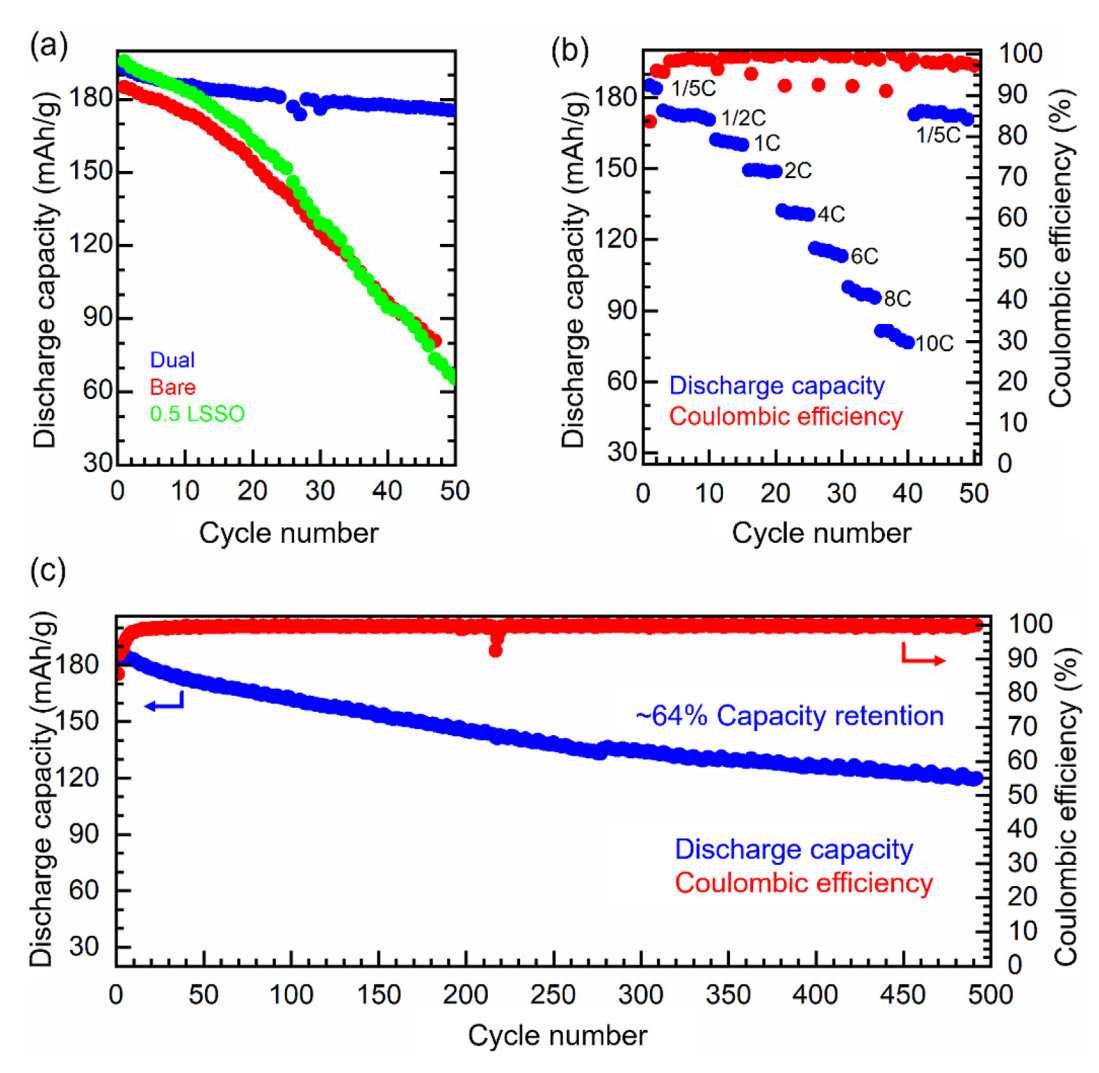


Fig. 1. (a) Short term cycling performance of uncoated LCO (bare) and coated 0.5 wt% LSSO (0.5 LSSO), 0.25 wt% LSSO, 0.25 wt% Al₂O₃ (Dual) LCO; (b) rate capability up to 10C and (c) long-term cycling for dual coated LCO.

and 50 cycled coated LCO. Ptychography measurements for pristine LCO show the same particle morphology as SEM (Fig. S5) and cycled samples reveal no noticeable change in the bulk particle morphology but display alterations at the surface of the particles. Fig. 3 shows elemental maps and ptychographic images for pristine and cycled electrodes coated with dual, 0.5 Al₂O₃, and 0.5 LSSO. Si and Sr elements were excluded because the particles were placed on Si₃N₄ membranes for measurements, and Sr L fluorescence signals were highly overlapped with Si (see Si and Sr L elemental maps in Fig. S6). The Al fluorescence map of the pristine LCO particle with dual coating in Fig. 3(a) shows a uniform distribution of coating on the boundary. A decrease in Al intensity at the left side is because the fluorescence detector was placed on the right side of the sample, and the Al fluorescence photons from the left edge were self-absorbed. This can also be observed in Si maps in Fig. S6, in which the particles blocked the Si signals from the substrate and created a shadow on the left side. The zoomed-in image at an edge area of the particle from the ptychographic image clearly shows a uniform layer of a coating with a thickness of about 100 nm. After cycling, the Al of the dual coating at particle boundary diffused slightly but still distributed mostly homogeneously across the whole particle. Ptychographic image also shows that the boundary between the coating and cathode particle is not as distinguishable as the pristine case after cycling, and the thickness of the coating layer in the example shown area varies from 100 to 200 nm. When the LCO particles were coated with 0.5 wt% Al₂O₃ the formation of a layer was evidenced by the Al maps in Fig. 3 (b). Ptychography of the pristine particle with Al₂O₃ coating gives a coating thickness of about 50 nm. The Al₂O₃ coating was still evident in the cycled particle in both the Al fluorescence map and ptychographic image. Fig. 3(c) shows that the particle with LSSO coating formed a uniform layer on the pristine particle surface with a thickness of about 50 nm. In addition, the ptychographic image of the cycled particle in Fig. 3(c) displays additional structures which do not have Co signals, which are presumably byproducts of the electrolyte. The fluorescence and ptychographic results imply that the coating scheme can effectively cover the surface of the cathode particles and prevent direct contact of the electrolyte with the cathode, which would decrease the battery performance. While the Al₂O₃ seems more stable, adding a layer of Al₂O₃ on LSSO can improve the performance of the coating.

Hard XAS (hXAS) at the Co K-edge was used to investigate the oxidation state and local structure of Co in the pristine LCO and cycled electrodes including bare, 0.5 Al₂O₃, 0.5 LSSO, and dual coated LCO [7,16,33,34]. Ex-situ measurements were performed on pristine material, and electrodes tested at 50 cycles. The 50 cycled cathodes show notable changes in the XANES depending on the surface coating or lack thereof. For example, compared to

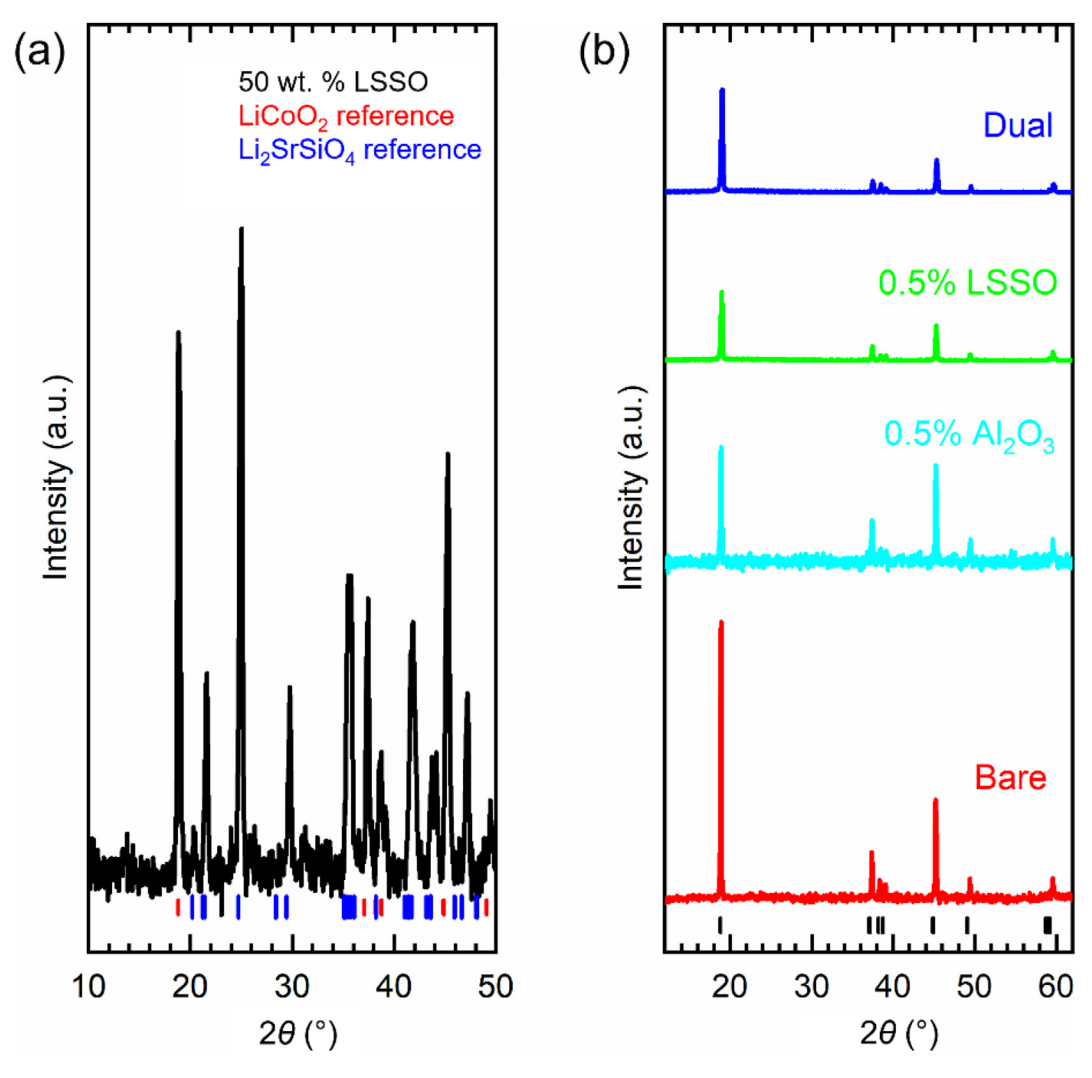


Fig. 2. X-ray diffraction of (a) excess LSSO coating (50 wt% LSSO) and (b) uncycled 0.5 wt% in total surface coatings on LCO.

the pristine LCO, the cycled bare LCO exhibits an edge shift of \sim 1 eV to higher energies, and the XANES spectrum aligns with the Co₃O₄ reference (Fig. 4a). Similarly, the underperforming coating of 0.5 LSSO also shifts by the same amount to higher energies, indicating the oxidation of Co from +3 to +4 [35-37]. Comparatively, such a shift is not observed for the high-performance coatings of 0.5 Al₂O₃ or the optimal dual coating, and the XANES edges of the two samples are well aligned with the uncycled pristine LCO. This finding indicates that Co ions' average oxidation state in these cathodes has remained in the normal state after 50 cycles [35–37]. This suggests that even thin coatings produced by sol-gel method, with some irregularities, can play a protective role and prevent degradation and eventual decline in performance and failure of cells. Further analysis of the EXAFS shows a similar local structure in the cycled samples to the pristine samples, consistent with XANES results in Fig. 4(b) and Fig. S7. Through hXAS we demonstrate that the bulk structure is not drastically changed.

Soft XAS (sXAS) in the electron yield mode is sensitive to the surface of the cathode particles with similar probing depths to XPS due to the short inelastic mean free path of the collected electrons [18,38,39]. Given that our coatings are on the nanometer scale, we measured XANES at the Co $L_{2,3}$ -edges and the O K-edge to understand what is occurring at the surface of the cathode particles. The Co L-edge spectra consist of a lower energy L_3 -edge at \sim 782 eV and a higher energy L_2 -edge at \sim 796 eV (L_2 -edge) which

are the result of electronic dipole transition from Co 2p to Co 3d states [38-40]. These transitions reflect the oxidation state of Co in the spectra by exhibiting shifts in the features or changes in the line shape. As shown in Fig. 5(a), the uncycled cathodes (coated and non-coated) exhibit an L_3 -edge at \sim 782 eV and an L_2 -edge at \sim 796 eV and have the consistent line shape of pristine LCO [39]. This rules out the possibility of thermally induced phase transitions in LCO during the coating process in agreement with XRD and XPS. Additionally, 50 cycled samples display a shift in the Ledges with the L_3 -edge at ${\sim}780$ eV and L_2 -edge at ${\sim}795$ eV. Furthermore, drastic changes in the spectral line shape of the Co L₃edge were observed. In Fig. 5(a), the change in spectra and the shift to lower energy indicate a reduction of Co from +3 to +2 [40]. This is because Co from the layered electrode leaches into the electrolyte during high voltage cycling, and it is well known that this occurs more readily in the +2 valence state. In our case, both the bare LCO and 0.5 Al₂O₃ display a higher degree of Co reduction, as indicated by the decreased overlap with the pristine LCO and the increase in the lower energy feature at \sim 779 eV. On the other hand, the 0.5 LSSO and dual samples display a greater degree of +3 cobalt; however, all cathodes show some degree of mixed oxidation +3/+2 on the surface [40].

Similar to the previous measurements, the O K-edge reveal that the uncycled materials retain the layered structure as they all have a strong feature at \sim 529 eV which corresponds to the electronic

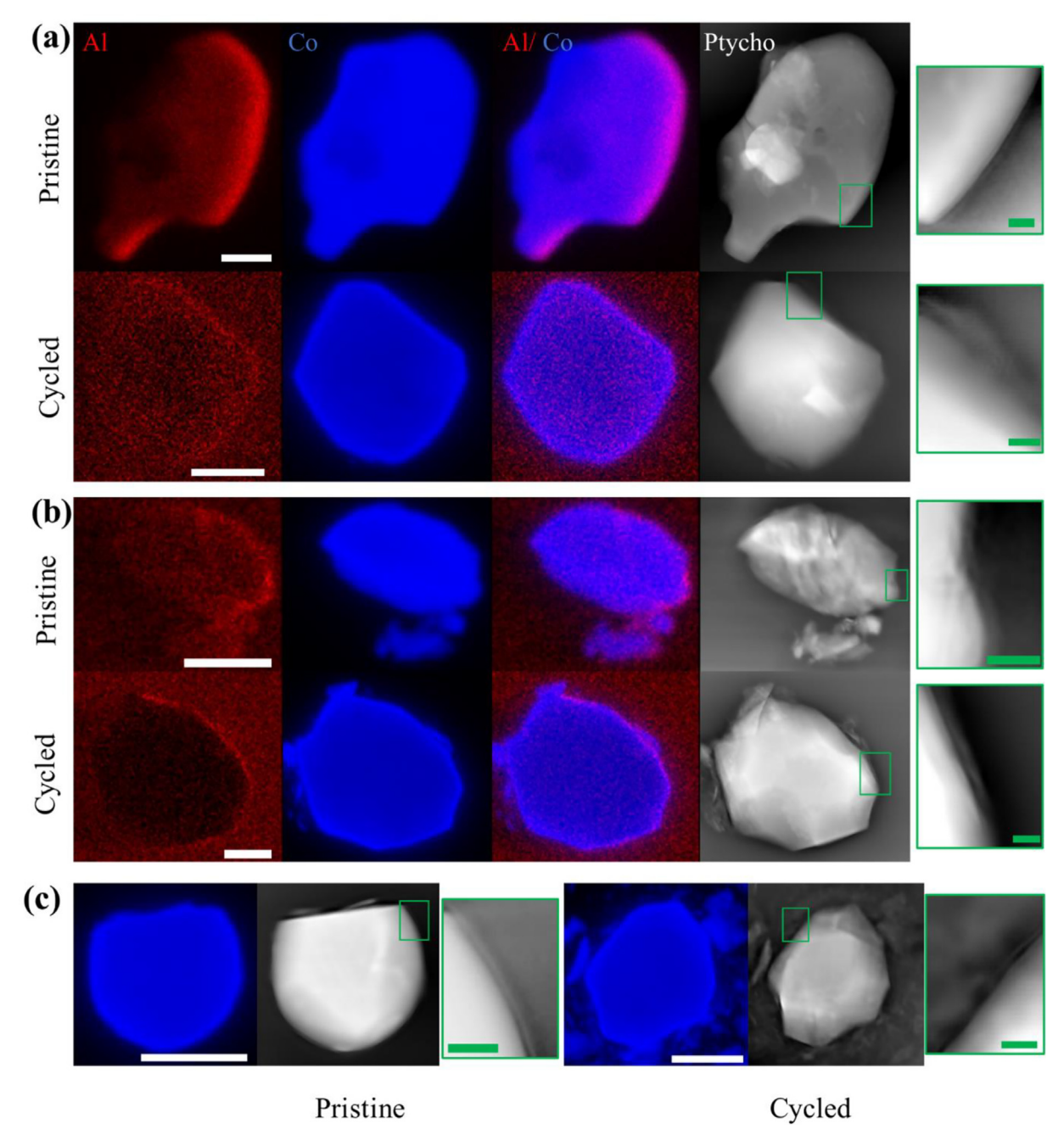


Fig. 3. X-ray fluorescence and ptychographic images for pristine and cycled electrodes coatings of (a) dual coating (0.25% LSSO & 0.25% Al₂O₃), (b) 0.5% Al₂O₃, and (c) 0.5% LSSO. The close-up images were taken from the areas marked by green boxes on ptychographic images to show the coating morphology. The scale bar (white) for the entire images is 5 µm, and the scale bar (green) of magnified images is 250 nm.

transitions from O 1s to O 2p–Co 3d orbital mixing found in LCO [38,39]. As expected, low intensity features from the surface coatings (Al $_2$ O $_3$ & LSSO) do appear in the spectra at \sim 531 eV for the uncycled cathodes 0.5 Al $_2$ O $_3$, 0.5 LSSO and dual samples. After cycling, the O K-edge spectra change dramatically due to the formation of a cathode-electrolyte interphase (CEI). After cycling, 0.5 Al $_2$ O $_3$, and dual coatings reveal the formation of a Li $_2$ CO $_3$ rich CEI as revealed by the similarity of the spectra to the LiCO $_3$ reference. The 0.5 LSSO and bare samples have spectra that differ from the other samples with a small intensity peak at \sim 531 eV and a broad feature near 537 eV. This suggests a different CEI that is unstable compared to the one formed 0.5 Al $_2$ O $_3$ and dual samples which show better performance.

4. Discussions

The synchrotron measurements provide great insight into the protective role of the coatings on the LCO. The ptychographic images with a spatial resolution of about 20 nm reveal a clear boundary around the perimeter of the as-coated cathode particles with a coating thickness ranging from 20–100 nm. Sufficient coverage of the cathode particles with a coating layer is needed to prevent direct contact of the electrolyte with the bare LCO since the uncoated LCO shows degrading performance when cycled to voltages greater than 4.2 V (Fig. 1a). After cycling, the thickness becomes non-uniform, and the distinction between the surface coating and cathode particle becomes blurred, indicating surface

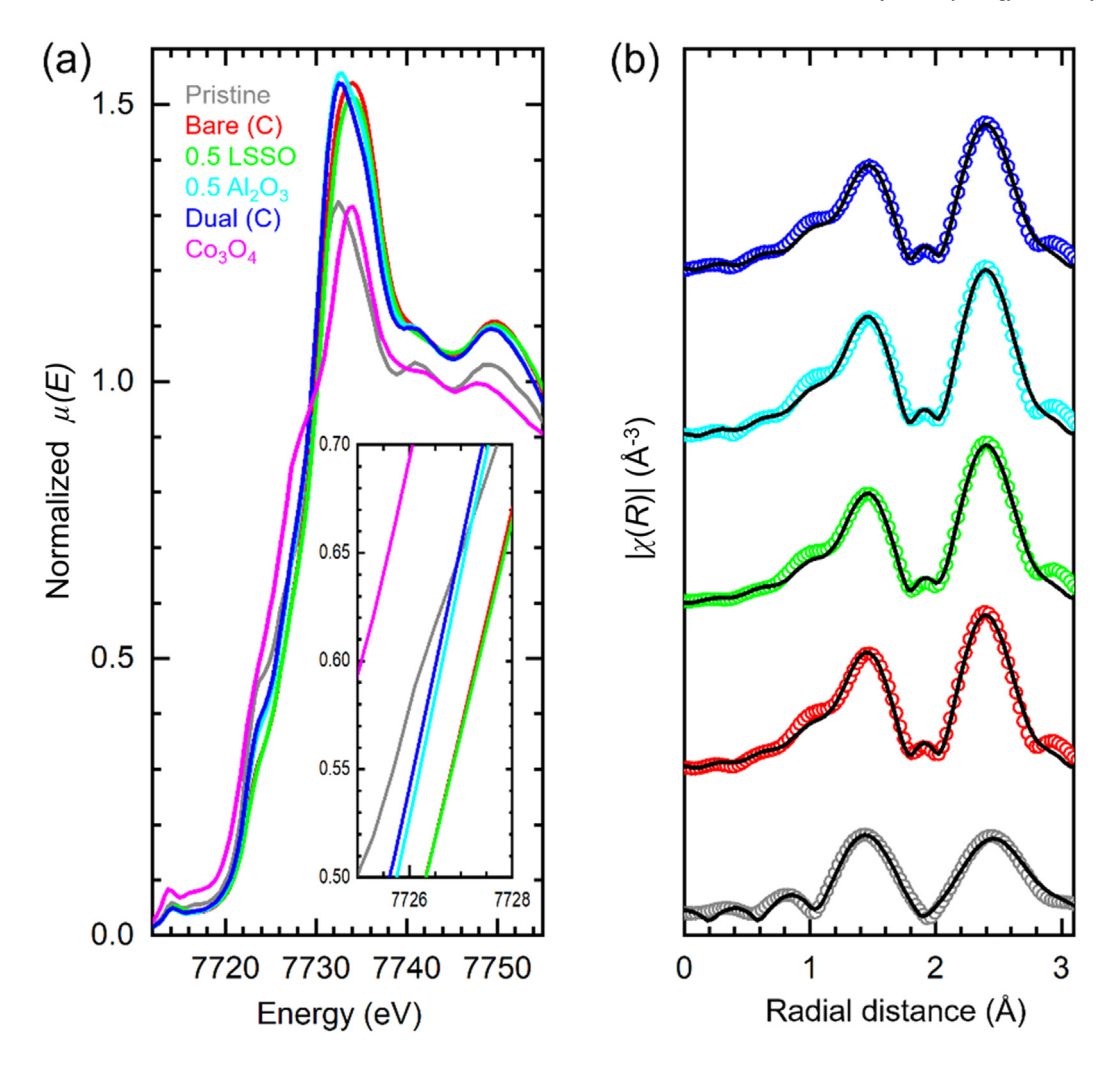


Fig. 4. Co K-edge XAS measurements including (a) XANES and (b) EXAFS of pristine bare (grey) and cycled (C) bare (red), 0.5 LSSO (green), 0.5 Al₂O₃ (cyan), and dual (blue) coated LCO.

reactions at the coating/cathode and coating/electrolyte interfaces (Fig. 3). These in-situ surface reactions can lead to different electrochemical performances and depend on the coating scheme on the LCO particles. In Fig. 1, this is observed in the dual coating, which leads to superior cycling performance compared to our other coatings. Fluorescence mapping provides further insight into the elemental distribution before and after cycling. In the as-coated state, we find the elements are in their expected position with Al on the perimeter of the LCO particles and Co in the center (Si and Sr L measurements were excluded due to the presence of Si in the sample holder and fluorescence signal overlap between Si and Sr L). As the battery is cycled, the bulk elemental distribution remains the same for the coated electrode materials. Although ptychography and X-ray fluorescence mapping can provide morphological and elemental distribution information, it lacks valence state information of the elements throughout the particles. Therefore, we turned to bulk and surface sensitive XAS to add another dimension of understanding to our system. Co K-edge hXAS, which probes hundreds of microns into the material, provides an ensemble average of the bulk environment of the LCO particles. As discussed previously, the uncoated and 0.5 LSSO samples displayed an edge shift while the 0.5 Al₂O₃ and dual samples retained an edge position similar to the pristine LCO. Shifts in the XANES are attributed to changes in the oxidation state of the absorbing atoms. We can conclude that uncoated and 0.5 LSSO samples undergo irre-

versible changes because of high voltage cycling, while the 0.5 Al₂O₃ and the dual coated samples have greater electrochemical reversibility. This increased reversibility could be due to the surface coating protecting the bulk by acting as a physical barrier and providing other functionalities such as HF scavenging and stable interphase formation, preventing major Co dissolution [24]. The theoretically superior HF scavenging ability of LSSO relative to Al₂O₃, due to numerous Si-O bonds, suggests that the failure of LSSO as an outer coating layer is due mainly to a failure to prevent the adsorption/degradation mechanisms of the electrolyte or other undesirable physical properties [18]. Therefore, its contribution to protecting the cathode by the dual coating is unlikely to be related to scavenging or preventing the production of HF in any significant way. This is because the role of the LSSO scavenging HF formed from the electrolyte must necessarily be reduced if it is present below a layer of Al₂O₃. The theoretical screening calculation by Aykol et al. [24] which served as the basis of this work, identified LSSO as a promising coating primarily of this HF scavenging ability and because of its likelihood of superior lithiumion conductivity. The role of LSSO in protecting active electrode material seems to be either due to its likely superior lithium-ion conduction or a chemical alteration to the Al₂O₃ layer. These potential chemical alterations to the Al₂O₃ layer may improve the lithium-ion conductivity or protection ability of the outer layer.

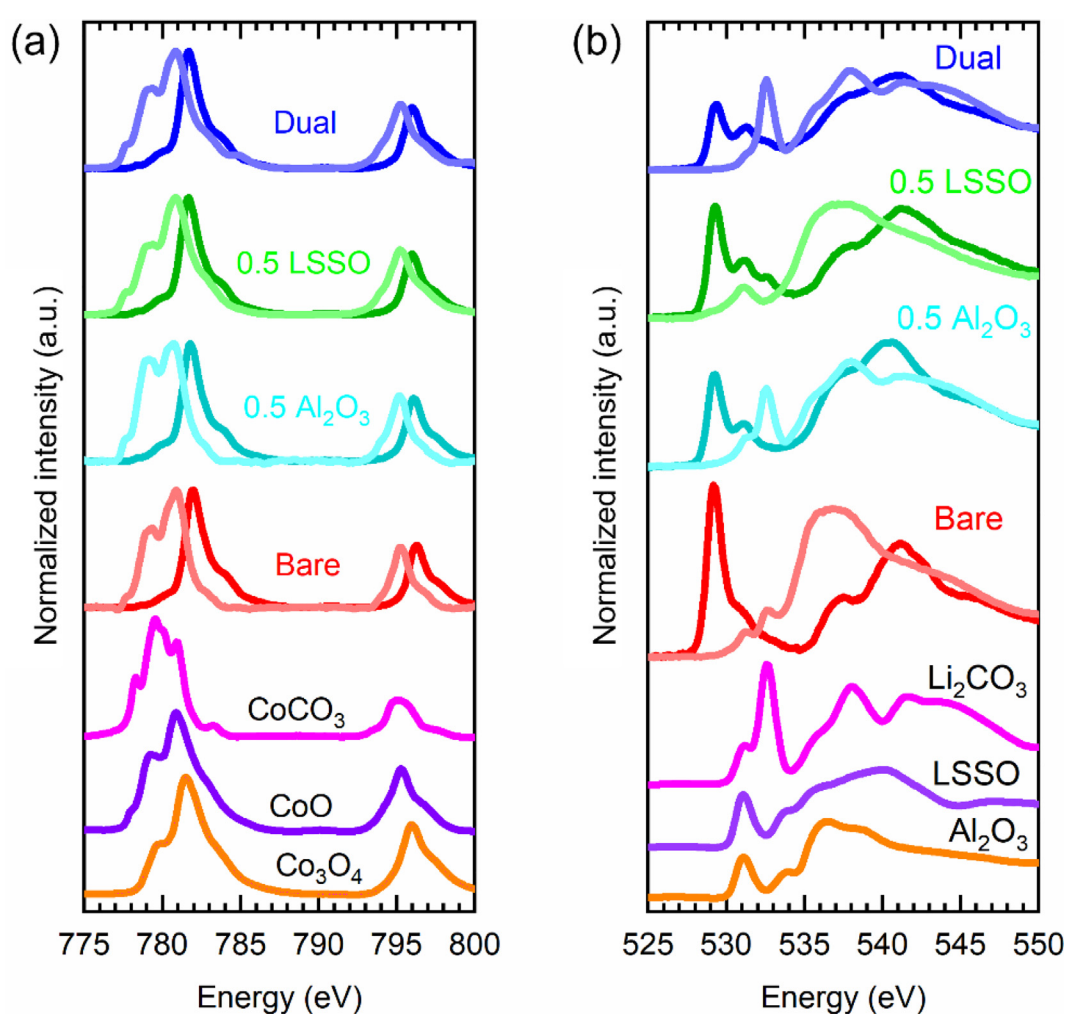


Fig. 5. Surface sensitive electron yield sXAS measurements at (a) Co L₂₋₃ edges and (b) O K-edge for uncycled (dark shade) and cycled (light shade) for bare (red), 0.5 Al₂O₃ (cyan), 0.5 LSSO (green) and dual (blue) coated LCO and select references (magenta, purple and orange).

Surface sensitive sXAS measurements further corroborate our hypothesis above. EY measurements at the Co L-edges and O Kedge provide elemental and compositional information for species at the surface of the electrode particles. We observe a Li₂CO₃ rich CEI formation for cycled 0.5 Al₂O₃ and dual coatings in the O Kedge. The similarity of the CEI in these two samples is due to the contact of Al₂O₃ with the electrolyte. In the uncoated, the CEI is composed of both Li₂O and LiCO₃, while 0.5 LSSO contains a thin CEI likely containing Li₂O. Due to the presence of Li₂O CEI, we suspect this does not support a stable interphase leading to degrading performance of the cells. The interphase is not the sole determining factor for improving the performance of the battery. The LSSO coating did not improve the cycling stability, but it did increase the cell's capacity, which could be caused by increasing the conductivity or lack of resistance growth at the interface. LSSO does not seem to form a thick interphase, which could be one contributing factor to the high signal of Co in fluorescence yield (FY) Co L-edge measurements (see Fig. S8). Similarly, in Fig. 5(a), the dual coating and LSSO reveal the oxidation state of Co in a state more similar to LCO. On the contrary, the Al_2O_3 and bare coating reveal increased reduction of Co as indicated by the increased intensity on the lower energy side of the spectra. The greater intensity of Co in FY could also signify less Co leaching for LSSO and the dual coating than the other coatings. Additionally, O K-edge for 0.5 LSSO showed no apparent CEI in the FY measurement, suggesting a thin

CEI layer (Fig. S8). This seems to suggest that the dual coating benefits from Al₂O₃ being the outer layer due to the formation of a stable CEI, while the inner layer of LSSO protects the cathode by preventing unstable CEI and prevents Co leaching. Furthermore, by simply applying the coating, all cells could appreciably prevent Co dissolution compared to the uncoated cycled LCO cells (Fig. S8).

The apparent insignificance of Sr in the functioning of the LSSO layer revealed by these characterization techniques, combined with the fact that Sr appears to be coated less homogeneously than Al, made us skeptical of the role of Sr in the function of the dual coating. To determine whether strontium has a role in the coating, we created dual coated LCO powder with Li₄SiO₄ (LSO) instead of Li₂SrSiO₄ using the same synthesis procedure but with more lithium in place of strontium. Li₄SiO₄ has been explored as a cathode coating before [21], as well as a solid-state electrolyte [18]. However, it appears to react with CO₂ [19], which is present as a decomposition byproduct in the electrolyte, and therefore even more readily with HF, meaning it may benefit from being partially shielded by an over-laying layer of Al₂O₃ to allow it to maintain itself and continue facilitating Li transport without electrodecoating reactions. LSO - Al₂O₃ coating powder resulted in nearly identical initial discharge capacity and long-term cyclability in half-cells to LSSO - Al₂O₃ (Fig. S9). This result further corroborates that the function of the LSSO in the dual coating is due to the properties of its lithium content and orthosilicate groups, not strontium, although further exploration of the LSO - Al_2O_3 dual coating is required to say for sure.

Looking back to the theoretical work [24] that sparked this investigation, Li₂SrSiO₄ may have been identified as an optimal coating material for layered cathode materials for reasons relating to its Sr content, which does not apply in the case of a dual coating. S-block elements containing species like Li₂SrSiO₄ appear to have been favored over species with similar structures and bonding characteristics, such as Li₄SiO₄ because they tend electrochemically inactive in the operating window of LIBs and form stable, HF scavenging oxides, even after they have previously reacted with HF [15]. Comparing LSO and LSSO, two things should be considered in the context of a dual coating. First, LSO should also be electrochemically stable, given the strength of the Si-O bonds and the resulting stability of the oxidation state of Si. Even upon irreversible discharge of Li₄SiO₄ itself, or reaction with electrolyte components, Li₂SiO₃ should be formed, containing lithium channels that facilitate good ionic conductivity [20]. Indeed, there have been publications on Li₂SiO₃ as a stand-alone cathode coating, [25] including a decent ranking as a coating in the theoretical work by Akyol et al. [24]. Secondly, the Sr-O theorized to continue scavenging HF after the decomposition of LSSO is less necessary when the layer of HF scavenging Al₂O₃ present on the surface of the LSSO is considered. Li₄SiO₄ also contains the same Si-O bonds for scavenging HF, so it seems that the additional HF scavenging and stability benefits of the Sr in LSSO are negligible. This being the case, replacing Sr with Li should continue to allow for potentially superior lithium transport while Si-O bonds scavenge HF. As a result, we suggest further research seek to refine the application of LSO -Al₂O₃ coatings (where LSO is either Li₂SiO₃ or Li₄SiO₄) rather than LSSO - Al₂O₃.

5. Conclusions

In this work, the coating of 0.25 wt% LSSO 0.25 wt% Al₂O₃ (dual coating) on LCO gives rise to improved electrochemical performance at a greater upper cut-off voltage of 4.5 V. compared to bare LCO, with an initial discharge capacity of 187 mAh/g, capacity retention of 64% after 500 cycles, and capacity utilization of 93% when returned to 0.5C after a 10C rate capability test. In addition, our dual coating can compete with and, in some cases, outperform LCO cells with higher cut-off voltages and more excellent coating uniformity in terms of capacity and long-term cycling stability (Table S2) [41–45]. We suspect the increased superior performance of the dual coating is due to the different functionalities of each single coating material (e.g., Al₂O₃ and LSSO). With a more ionically conductive and electrochemically stable inner layer, the LSSO will not react with the cathode. At the same time, the outer layer can protect the coated cathode by reacting with the electrolyte and producing a favorable CEI that prevents continued reactions and cathode degradation. The discrepancy between the theoretical basis by Aykol et al. [24] and the observed results appears to be mainly due to the different components of the CEI formed by LSSO than by Al₂O₃ upon charging to a high cut-off voltage. It may be possible that LSSO is a much better electronic conductor than Al₂O₃, which was also not considered in the screening study and could allow for electrolyte oxidation by the cathode at over 4.2 V. Bulk sensitive methods (XRD, hXAS, and FY sXAS) confirm that there are minimal changes in the bulk environment, and therefore, the coatings act mainly at the surface. Surface sensitive EY sXAS data corroborate our hypothesis of the function of the dual coating on the surface of LCO, showing reduced detrimental cobalt reduction in LSSO coated material, but a Li₂CO₃ containing CEI that forms primarily in Al₂O₃ and dual coated materials. The X-ray fluorescence, ptychographic imaging and XRD data collected, demonstrate the efficacy of sol-gel methods for the application of complex inorganic coatings like LSSO. Future work should seek to identify single coating species that can offer the different properties of LSSO and Al₂O₃ simultaneously so that only one coating must be applied to the surface of cathode particles. Such coatings should be applied via scalable wet chemistry techniques to demonstrate scalability and explore more complex compositions. Ideal coatings should scavenge HF, be ionically conductive but electronically insulating, and have positive reaction energies with the cathode species.

Declaration of Competing Interest

The authors declare that they have no known competing financial interests or personal relationships that could have appeared to influence the work reported in this paper.

Acknowledgments

This work was supported by the U.S. National Science Foundation (CBET-1949870, CBET-2016192, and DMR-1832803). Part of the research was conducted at the Northwest Nanotechnology Infrastructure, a National Nanotechnology Coordinated Infrastructure (NNCI) site at Oregon State University, which is supported, in part, by the U.S. National Science Foundation (NNCI-1542101 and NCC-2025489), and Oregon State University. This research used resources of the Advanced Photon Source at ANL, Advanced Light Source at Lawrence Berkeley National Laboratory and National Synchrotron Light Source II at Brookhaven National Laboratory, which are U.S. DOE Office of Science User Facilities under contract No. DE-AC02-06CH11357, DE-AC02-05CH11231, and DE-SC0012704, respectively. The authors would like to thank Cherno Jaye and Daniel A. Fischer at NSLS II for help in data collection and Dr. Xiaolin Li for useful discussions.

Appendix A. Supplementary data

Supplementary data to this article can be found online at https://doi.org/10.1016/j.jechem.2021.11.014.

References

- K. Mizushima, P.C. Jones, P.J. Wiseman, J.B. Goodenough, Solid State Ionics. 3–4 (1981) 171–174.
- [2] A. Yoshino, Angew. Chem. Int. Ed. 51 (2012) 5798-5800.
- [3] C. Pillot, The Rechargeable Battery Market and Main Trends 2018–2030, Avicenne Energy, Berlin, 2019.
- [4] W. Cole, A.W. Frazier, Cost Projections for Utility-Scale Battery Storage: 2020 Update, National Renewable Energy Laboratory, Golden, CO, 2020.
- [5] M.S. Ziegler, J.E. Trancik, Energy Environ. Sci. 14 (2021) 1635–1651.
- [6] G. Patry, A. Romagny, S. Martinet, D. Froelich, Energy Sci. Eng. 3 (2014) 71–82.
- [7] M. Lucero, S. Qiu, Z. Feng, Carbon Energy 3 (2021) 762-783.
- [8] A. Manthiram, Nat. Commun. 11 (2020) 1550–1558.
- [9] T.M.M. Heenan, A. Wade, C. Tan, J.E. Parker, D. Matras, A.S. Leach, J.B. Robinson, A. Llewellyn, A. Dimitrijevic, R. Jervis, P.D. Quinn, D.J.L. Brett, P.R. Shearing, Adv. Energy Mat. 10 (2020) 2002655.
- [10] H. Li, A. Liu, N. Zhang, Y. Wang, S. Yin, H. Wu, J.R. Dahn, Chem. Mater. 31 (2019) 7574–7583.
- J.M. Lim, T. Hwang, D. Kim, M.S. Park, K. Cho, M. Cho, Sci. Rep. 7 (2017) 39669.
 E. Zhitao, H. Guo, G. Yan, J. Wang, R. Feng, Z. Wang, X. Li, J. Energy Chem. 55 (2021) 524–532.
- [13] G.G. Amatucci, J.M. Tarascon, L.C. Klein, Solid State Ionics 83 (1995) 167–173.
- [14] Z. Jian, W. Wang, M. Wang, Y. Wang, N. AuYeung, M. Liu, Z. Feng, Chin. Chem. Lett. 29 (2018) 1768–1772.
- [15] N.V. Faenza, L. Bruce, Z.W. Lebens-Higgins, I. Plitz, N. Pereira, L.F.J. Piper, G.G. Amatucci, J. Electrochem. Soc. 164 (2017) A3727–A3741.
- [16] Z. Feng, In-situ synchrotron X-ray characterizations of battery materials. in: Encyclopedia of Energy Storage, Elsevier, 2021, pp. 1–13.
- [17] M. Liu, J. Vatamanu, X. Chen, L. Xing, K. Xu, W. Li, ACS Energy Lett. 6 (2021) 2096–2102.
- [18] H. Gao, X. Zeng, Y. Hu, V. Tileli, L. Li, Y. Ren, X. Meng, F. Maglia, P. Lamp, S.-J. Kim, K. Amine, Z. Chen, A.C.S. App, Energy Mater. 1 (2018) 2254–2260.

- [19] F. Schipper, H. Bouzaglo, M. Dixit, E.M. Erickson, T. Weigel, M. Talianker, J. Grinblat, L. Burstein, M. Schmidt, J. Lampert, C. Erk, B. Markovsky, D.T. Major, D. Aurbach, Adv. Energy Mater. 8 (2018) 1701682.
- [20] A. Yano, M. Shikano, A. Ueda, H. Sakaebe, Z. Ogumi, J. Electrochem. Soc. 164 (2016) A6116–A6122.
- [21] A.M. Wise, C. Ban, J.N. Weker, S. Misra, A.S. Cavanagh, Z. Wu, Z. Li, M.S. Whittingham, K. Xu, S.M. George, M.F. Toney, Chem. Mater. 27 (2015) 6146–6154.
- [22] Y. Oh, D. Ahn, S. Nam, B. Park, J. Solid State Electrochem. 14 (2009) 1235–1240.
- [23] S. Xu, R.M. Jacobs, H.M. Nguyen, S. Hao, M. Mahanthappa, C. Wolverton, D. Morgan, J. Mater. Chem. A. 3 (2015) 17248–17272.
- [24] M. Aykol, S. Kim, V.I. Hegde, D. Snydacker, Z. Lu, S. Hao, S. Kirklin, D. Morgan, C. Wolverton, Nat. Commun. 7 (2016) 13779.
- [25] Y.S. Jung, P. Lu, A.S. Cavanagh, C. Ban, G.-H. Kim, S.-H. Lee, S.M. George, S.J. Harris, A.C. Dillon, Adv. Energy Mater. 3 (2013) 213–219.
- [26] R.W. Johnson, A. Hultqvist, S.F. Bent, Mater. Today 17 (2014) 236-246.
- [27] J. Deng, D.J. Vine, S. Chen, Y.S. Nashed, Q. Jin, N.W. Phillips, T. Peterka, R. Ross, S. Vogt, C.J. Jacobsen, Proc. Natl. Acad. Sci. USA 112 (2015) 2314–2319.
- [28] J. Deng, Y.H. Lo, M. Gallagher-Jones, S. Chen, A.P. Jr, Q. Jin, Y.P. Hong, Y.S.G. Nashed, S. Vogt, J. Miao, C. Jacobsen, Sci. Adv. 4 (2018) eaau4548.
- [29] Z. Chen, J.R. Dahn, Electrochem. Solid-State Lett. 6 (2003) A221-A224.
- [30] L. Liu, L. Chen, X. Huang, X.-Q. Yang, W.-S. Yoon, H.S. Lee, J. McBreen, J. Electrochem. Soc. 151 (2004) A1344–A1351.
- [31] M. Wang, Z. Feng, Chem. Comm. 57 (2021) 10453-10468.
- [32] L. Dahéron, R. Dedryvère, H. Martinez, M. Ménétrier, C. Denage, C. Delmas, D. Gonbeau, Chem. Mater. 20 (2008) 583–590.

- [33] M. Wang, L. Árnadóttir, Z.J. Xu, Z. Feng, Nano-Micro Lett. 11 (2019) 47.
- [34] M. Wang, Z. Feng, Curr. Opin. Electrochem. 30 (2021) 100803–100809.
- [35] D. Takamatsu, Y. Koyama, Y. Orikasa, S. Mori, T. Nakatsutsumi, T. Hirano, H. Tanida, H. Arai, Y. Uchimoto, Z. Ogumi, Angew. Chem. Int. Ed. 51 (2012) 11597–11601.
- [36] I. Nakai, K. Takahashi, Y. Shiraishi, T. Nakagome, F. Izumi, Y. Ishii, F. Nishikawa, T. Konishi, J. Power Sources. 68 (1997) 536–539.
- [37] L. Chen, X. Fan, E. Hu, X. Ji, J. Chen, S. Hou, T. Deng, J. Li, D. Su, X. Yang, C. Wang, Battery. Chem. 5 (2019) 896–912.
- [38] C.-H. Chen, B.-J. Hwang, C.-Y. Chen, S.-K. Hu, J.-M. Chen, H.-S. Sheu, J.-F. Lee, J. Power Sources. 174 (2007) 938–943.
- [39] W.-S. Yoon, K.-B. Kim, M.-G. Kim, M.-K. Lee, H.-J. Shin, J.-M. Lee, J.-S. Lee, C.-H. Yo, J. Phys. Chem. 106 (2002) 2526–2532.
- [40] S. Li, K. Li, J. Zheng, Q. Zhang, B. Wei, X. Lu, J. Phys. Chem. Lett. 10 (2019) 7537–7546.
- [41] Y.-K. Sun, C.S. Yoon, S.-T. Myung, I. Belharouak, K. Amined, J. Electrochem. Soc. 156 (2009) A1005–A1010.
- [42] H. Miyashiro, A. Yamanaka, M. Tabuchi, S. Seki, M. Nakayama, Y. Ohno, Y. Kobayashi, Y. Mita, A. Usami, M. Wakiharac, J. Electrochem. Soc. 153 (2006) A348–A353.
- [43] S.S. Jayasree, D.S. Nair, D.D. Santhanagopalan, ChemistrySelect. 3 (2018) 2763–2766.
- [44] J. Xie, J. Zhao, Y. Liu, H. Wang, C. Liu, T. Wu, P.-C. Hsu, D. Lin, Y. Jin, Y. Cui, Nano Res. 10 (2017) 3754–3764.
- [45] T. Cheng, Z. Ma, R. Qian, Y. Wang, Q. Cheng, Y. Lyu, A. Nie, B. Guo, Adv. Funct. Mater. 31 (2020) 2001974.